

# Spectral index of the Galactic foreground emission in the 50 – 87 MHz range

M. Spinelli<sup>1,2\*</sup>, G. Bernardi<sup>3,4,5</sup>, H. Garsden<sup>6</sup>, L.J. Greenhill<sup>6</sup>, A. Fialkov<sup>7,8</sup>

J. Dowell<sup>9</sup> and D.C. Price<sup>6,10</sup>

<sup>1</sup>INAF-Osservatorio Astronomico di Trieste, Via G.B. Tiepolo 11, 34143 Trieste, Italy

<sup>2</sup>IFPU - Institute for Fundamental Physics of the Universe, Via Beirut 2, 34014 Trieste, Italy

<sup>3</sup>INAF-Istituto di Radioastronomia, via Gobetti 101, 40129, Bologna, Italy

<sup>4</sup>Department of Physics & Electronics, Artillery Road, Rhodes University, Grahamstown, South Africa

<sup>5</sup>South African Radio Astronomy Observatory, FIR street, Observatory, Cape Town, South Africa

<sup>6</sup>Harvard-Smithsonian Center for Astrophysics, 60 Garden Street, Cambridge MA 02138 USA

<sup>7</sup>Kavli Institute for Cosmology, Madingley Road, Cambridge CB3 0HA, UK

<sup>8</sup>Institute of Astronomy, University of Cambridge, Madingley Road, Cambridge CB3 0HA, UK

<sup>9</sup>University of New Mexico, 1919 Lomas Boulevard NE, Albuquerque, NM 87131, USA

<sup>10</sup>International Centre for Radio Astronomy Research, Curtin University, Bentley WA 6102, Australia

May 17, 2022

## ABSTRACT

Radiometry using individual dipole antennas is a potentially effective way to study the cosmological epoch referred to as Cosmic Dawn ( $z \sim 20$ ) through measurement of sky brightness arising from the 21 cm transition of neutral hydrogen, provided this can be disentangled from much stronger Galactic and extragalactic foregrounds. In the process, measured spectra of integrated sky brightness temperature can be used to quantify properties of the foreground emission. In this work we analyze data from the Large-aperture Experiment to Detect the Dark Age (LEDA) in the range 50–87 MHz to constrain the spectral index  $\beta$  of foreground emission in the northern sky visible at mid-latitudes. We focus on two zenith-directed LEDA radiometers and study how estimates of  $\beta$  vary with local sidereal time (LST). We correct for the effect of gain pattern chromaticity and compare estimated absolute temperatures with simulations. During times with the best observing conditions, for a “reference” radiometer whose configuration was fixed throughout the observing interval, we estimate that  $\beta$  varies from  $-2.55$  to a steeper  $-2.58$ , consistent with previous measurements of the southern sky and simulated sky models. Using data from the second, experimental, radiometer, we observe a similar trend vs. LST although with slightly smaller  $|\beta|$ , in the  $-2.46 < \beta < -2.43$  range. We infer good instrument stability from consistency in computed spectral indices at a level of  $1-2\sigma$  for  $LST = 9 - 12.5$  h, using data gathered during campaigns distributed between mid-2018 to mid-2019. Evidence for spectral curvature is weak owing to residual systematic errors, other than when the Galactic Center is in the sky, at which time we find evidence for negative curvature,  $\gamma \sim -0.4$ . The timing of occasional shifts in the temperature scales of the two widely spaced radiometers suggests substantial sensitivity to the water content of the sandy soil.

**Key words:** dark ages, reionization, first stars - Galaxy: structure - instrumentation: miscellaneous

## 1 INTRODUCTION

The challenging measurement of a signal from the Cosmic Dawn of the Universe finds its most promising observable in the 21 cm line of the neutral Hydrogen (e.g., Furlanetto et al. 2006; Pritchard & Loeb 2010). At Cosmic Dawn, Ly- $\alpha$  photons, produced by the first stars, couple the excitation temperature of the 21 cm line to the gas kinetic temperature through the Wouthuysen-Field effect (WF, Wouthuysen 1952; Field 1958), producing a negative contrast against the Cosmic Microwave Background (CMB) temperature and thus an absorption signal. Eventually, the progress of structure formation through grav-

itational collapse completely couples the spin temperature to the gas temperature. As a consequence of gas heating, most likely by an X-ray background, the gas/spin temperature is then driven well above the CMB temperature (e.g., Venkatesan et al. 2001; Pritchard & Furlanetto 2007; Mesinger et al. 2013). The interplay between Ly- $\alpha$  coupling and X-ray heating is thus expected to create a few hundreds mK absorption features in the *global - i.e. sky averaged* - 21 cm signal, sensitive to the formation of the first luminous structures in the Universe (e.g., Barkana & Loeb 2005; Furlanetto et al. 2006; Fialkov et al. 2013; Mirocha 2014; Mesinger et al. 2016; Mirocha & Furlanetto 2019), and to the thermal history of the intergalactic medium (Pritchard & Furlanetto 2007; Mesinger et al. 2013; Fialkov et al. 2014).

\* E-mail: marta.spinelli@inaf.it

In principle, the global 21 cm signal can be measured with a single antenna and noise-switched receiver in  $O(10^2)$  hours (e.g., Shaver et al. 1999; Bernardi et al. 2015; Harker et al. 2016). The Experiment to Detect the Global Epoch-of-Reionization Signatures (EDGES) team has claimed detection of a broad absorption profile peaking at  $-520$  mK and centered at 78 MHz (Bowman et al. 2018). This is more than a factor two deeper than predicted from theory based on standard physics (e.g. Cohen et al. 2017). If the EDGES signal is confirmed to be of cosmological origin, it implies that either the temperature of the radio background is higher than that of the CMB (e.g. Bowman et al. 2018) or the neutral gas at  $z \sim 17$  is colder than expected (e.g. due to interactions with cold dark matter, Barkana 2018). The flat line profile is also novel.

Subsequent analysis by other authors have suggested the existence of a residual unmodeled systematic sinusoidal feature in EDGES data (Hills et al. 2018; Singh & Subrahmanyan 2019; Bevins et al. 2020) that could modify their best fit parameters. Similarly, Spinelli et al. (2019) suggested an unaccounted for contamination from polarized foregrounds. Moreover, using Bayesian evidence-based comparison, Sims & Pober (2020) found no strong evidence in favor of models including a global 21 cm. The importance and the implications of the EDGES result need confirmation from another independent experiment to be fully convincing against criticisms.

The effort to measure the global 21 cm signal has been ongoing for several years with variegated instrumental designs. The Large aperture Experiment to detect the Dark Ages (LEDA; Price et al. 2018), whose latest data are analyzed in this work, constrained at 95% confidence level the amplitude ( $> -890$  mK) and the  $1\sigma$  width ( $> 6.5$  MHz) of a Gaussian model for the trough (Bernardi et al. 2016). Moreover, the upgraded Shaped Antenna measurement of the background RAdio Spectrum (SARAS 3) has provided constraints in the  $6 < z < 10$  range (Singh et al. 2017, 2018); the “Sonda Cosmologica de las Islas para la Detección de Hidrogeno Neutro (SCI-HI; Voytek et al. 2014) reported a 1 K root mean square (RMS) residual in the range 60 – 88 MHz. Other experiments are the Probing Radio Intensity at high-Z from Marion (PRIZM) experiment (Philip et al. 2019), the Broadband Instrument for Global HydrOgen ReioNisation Signal (BIGHORNS; Sokolowski et al. 2015) and the Radio Experiment for the Analysis of Cosmic Hydrogen (REACH)<sup>1</sup>. Moreover, there are proposals (e.g. the Dark Ages Polarimeter Pathfinder [DAPPER]<sup>2</sup>) to measure the 21 cm global signal from the orbit of the moon to avoid terrestrial radio frequency interference, ionospheric corruption and solar radio emissions.

The key challenge to measuring the 21 cm signal is the subtraction of the bright foregrounds. The low-frequency radio sky is a superposition of several components including galactic synchrotron and free-free emission, supernova remnants, radio galaxies and absorption from HII regions. Galactic and extra-galactic synchrotron and free-free emissions have typical sky temperature of thousands of K at 75 MHz, several orders of magnitude stronger than the pristine Cosmic Dawn signal. The proper characterization of the foreground emission thus plays a fundamental role in the 21 cm global signal analysis. Current modeling often uses extrapolations of the all-sky 408 MHz survey of Haslam et al. (1982) to lower frequencies. Other more sophisticated models are available: an improved version of the Global Sky Model (GSM, De Oliveira-Costa et al. 2008; Zheng et al. 2016), including Parkes telescope maps at 150 MHz and 85 MHz

(Landecker & Wielebinski 1970); the Global MOdel for the radio Sky Spectrum (GMOSS, Sathyanarayana Rao et al. 2017) for the low-frequency radio sky from 22 MHz to 23 GHz. However, the majority of information contained in these models is derived at high frequencies. Other measurements are available: Guzmán et al. (2011) produced a Galactic large-scale synchrotron emission temperature map at 45 MHz covering more than 95% of the sky; the northern hemisphere has been covered by the Long Wavelength Array (LWA)-1 Low-Frequency Sky Survey (Dowell et al. 2017) at a range of frequencies between 35 and 80 MHz with few degree resolution. These maps are not in complete agreement with the GSM at the same frequencies, probably due to an increased contribution of free-free absorption (Dowell et al. 2017). Eastwood et al. (2018) released low-frequency maps of the full sky visible from the Owens Valley Radio Observatory (OVRO) between  $\sim 36$  and  $\sim 73$  MHz. OVRO-LWA maps have  $15'$  angular resolution thus complementing the existing full-sky maps at these frequencies, but being exclusively from interferometric observations, they do not represent the globally averaged sky brightness.

Global signal experiments, while targeting the Cosmic Dawn, can contribute to the knowledge of the low-frequency radio sky: with their large beams they average the absolute sky brightness temperature over large spatial scales. The diffuse and continuum foreground sources are known to be spectrally smooth; that is, they should exhibit power-law spectra<sup>3</sup> over the low frequency band of interest. Measurements of the Galactic foreground spectral index  $\beta$  have been obtained with single dipole antennas. Rogers & Bowman (2008) found, for the frequency range 100 – 200 MHz, that the spectral index of diffuse emission was  $\beta = -2.5 \pm 0.1$  at high-Galactic latitudes. Patra et al. (2015), using the SARAS experiment, measured the spectral index in the 110 – 170 MHz band covering the 23 – 1 h local sidereal time (LST) range. They reported a slow variation with LST and a steepening from  $-2.3$  to  $-2.45$  when observing off the Galactic center. In Mozdzen et al. (2017) the EDGES team obtained a measurement of the spectral index in the southern hemisphere, in the frequency range 90 – 190 MHz. They found  $-2.60 > \beta > -2.62$  in the 0 – 12 h LST range, with an increase up to  $\beta = -2.50$  at 17.7 h, when the Galactic center is transiting. In the 50 – 100 MHz range, Mozdzen et al. (2019) found the spectral index to be  $-2.59 < \beta < -2.54$  for LST values below 12 h and a flattening to  $-2.46$  when the Galactic center transits. Moreover, exploiting a lunar occultation technique with the Murchison Widefield Array telescope, McKinley et al. (2018) measured a spectral index of  $-2.64 \pm 0.14$ , at the position of the Moon, in the frequency range 72 – 230 MHz.

The LEDA experiment covers instead the full northern hemisphere, offering an important complementary measure of the spectral index. Price et al. (2018), using LEDA data from 40 to 83 MHz, found that the spectral index varies between  $-2.28$  to  $-2.38$  over the full LST range.

In this work, we present new results on the spectral index of the Galactic foreground emission in the 50 – 87 MHz range using the latest LEDA measurements, covering  $\sim 140$  nights distributed between mid-2018 to mid-2019.

The paper is organized as follows. In Section 2 we describe LEDA observation and data processing, and we assess the quality of our data. In Section 3.3 we present our beam model and correct for the effect of its chromatic response. This is an important step to correctly evaluate the spectral index that was not performed in previous LEDA analysis. In Section 4 we apply a global temperature scale correction

<sup>1</sup> <http://www.astro.phy.cam.ac.uk/research/research-projects/reach>

<sup>2</sup> <https://www.colorado.edu/project/dark-ages-polarimeter-pathfinder>

<sup>3</sup>  $T(\nu) \propto \nu^\beta$

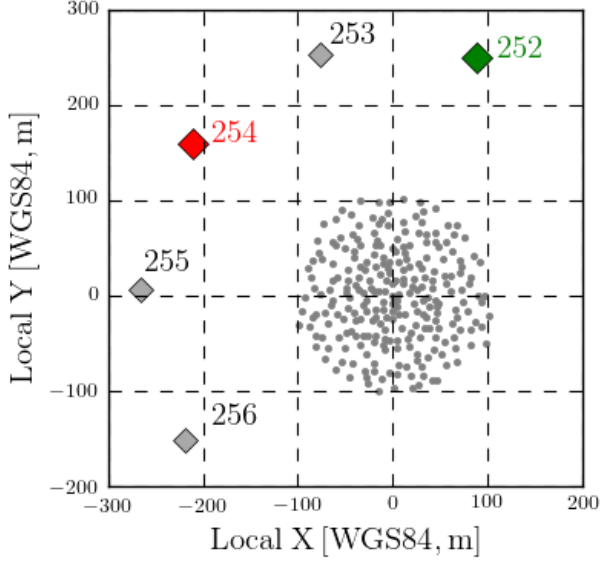


**Figure 1.** OVRO-LWA antenna positions in WGS84 coordinates relative to the center. Diamonds represent the LEDA outrigger stands, positioned at distance to minimize mutual couplings effects. We highlight in color the two antennas used in this analysis, the 254 in red and the 252 in green.

to the data to overcome some systematic effects and to match our spectra with the expected sky temperature. Our results are presented in Section 5, followed by discussion and conclusions in Section 7.

## 2 OBSERVATIONS AND DATA PROCESSING

A detailed description of the LEDA system can be found in Kocz et al. (2015) and Price et al. (2018). We briefly summarize here the relevant details together with describing relevant changes to the system performed after Price et al. (2018) was published. LEDA dual polarization radiometric receivers are installed in place of LWA receivers on a subset of antennas within OVRO-LWA ( $37^{\circ} 14' 23.1998''$  N,  $118^{\circ} 16' 53.9995''$  W). For the purposes of this work we use these “LEDA antennas”, which are  $\sim 170$  m away ( $\sim 42 \lambda$  at 75 MHz) from other LWA antennas so as to limit mutual coupling effects. The array layout is shown in Figure 1. Each dual-polarization antenna comprises two pairs of triangular dipole arms, 1.4 m angled downward by  $45^{\circ}$ . The orientation of the east-west dipole axis defines polarization A, and the other polarization B. The vertex of the antenna is 1.5 m off the ground.

In this analysis we report on results using polarization A from antennas 252 and 254. In order to minimize the effect of the ambient conditions on the dipole beam pattern, both antennas were first equipped with a  $3 \text{ m} \times 3 \text{ m}$  ground screen, comprising 12.5 mm gauge welded galvanized wire with a 10.2 cm spacing. After January 2019, the ground screen on antenna 252 was replaced by a  $20 \text{ m} \times 20 \text{ m}$  ground screen, comprised of an 11 mm gauge wire arranged in a 10 m square with serrations created by four 5 m-long isosceles triangles on each side (see Figure 2). The serrations are intended to attenuate the effect of the mismatch between the ground and the screen along the edge.

New receiver filters were also installed in order to extend the useful band up to 87.5 MHz.

Observations span a total of 137 nights, with 120 nights distributed from December 2018 to May 2019, and 17 nights in May 2018 as a further control sample for data stability with time.

Data were collected with a 24 kHz frequency resolution, over the 30 – 87.5 MHz range, and radio frequency interference was excised with an iterative thresholding method (Offringa et al. 2010; Price et al. 2018). They were calibrated via a three-position switch, which loops between the sky, a cold and a hot load every 5 s, for an actual 30% time duty cycle on the sky. Spectra are further corrected for reflection coefficients measured in the lab (Price et al. 2018).

As we will discuss further in Section 4, the Galactic plane contributes significantly to the overall system temperature of zenith-directed low-frequency radiometers, so, for aiming at a detection of the 21 cm signal, it is better to observe when the brightest portions of the plane are low in the sky. As well, the consistency of low-frequency radiometer performance depends in part on the environment, the effect of variable soil moisture on complex permittivity being prominent. Seasonal dry conditions in 2018 carrying over from summer persisted into the first half of January 2019. Consequently, we anticipate data acquired in December 2018 and January 2019 to be the best. Unusually heavy winter rains thereafter posed challenges to be addressed in later sections. For the purposes of a more complete analysis of the foreground spectral index, we extend the analysis of these December/January data to nearly 24 h (i.e., including sidereal times when bright Galactic emission is high in the sky). This constitutes our *reference* dataset.

In Figure 3 we present, for illustrative purposes, 24 h observation from December 2018. We can appreciate variations in the foreground amplitude as a function of LST.

### 2.1 Statistics of data integration and noise levels

At frequencies below  $\sim 50$  MHz, where the wavelength is twice the size of the default  $3 \times 3$  m ground screen configuration, spectra change noticeably over time scales of a few days, likely due to the instrument sensitivity to environmental effects. We therefore discarded data below 50 MHz, retaining 1540 of the original 2400 channels.

For a single frequency channel, the measured temperature varies over time and includes random Gaussian noise,  $T(t) + n$ . Assuming the noise in each channel to be distributed as a Gaussian with mean  $\mu_n = 0$  and standard deviation  $\sigma_n$ , it is possible to estimate the noise variance by removing  $T(t)$ . We de-trend the signal using a mean filter with a sliding-window of  $\sim 4$  minute width (16 data points) to this aim. This procedure does not inject correlation into the data, but the uncertainties will be partially correlated over the 4 minute interval. Once  $T(t)$  is removed, we verify that the extracted noise is Gaussian distributed and estimate the variance  $\sigma_n$  of the distribution. In the range of frequencies we are interested in for our analysis, the  $\sigma_n$  values per channel are around tens of Kelvin.

We averaged the signal over 1 MHz-wide channels, using the variance computed in each channel as a weight. The typical noise in a 1 MHz channel is a few Kelvin at 75 MHz for a 5 s integration time. These 1 MHz spectra are the ones used in our analysis.

### 2.2 Stability and consistence

The observed temperature varies as a function of LST as the foreground sky changes as observed by a fixed antenna, however, it is ideally the same if measured at the same LST over different days. Figure 4 shows how the observed temperature (for 1 h integration time around LST 12 h) varies over the course of our observations. For





**Figure 2.** LEDA outrigger antenna 252 (left) and 254 (right) installed at OVRO-LWA. The antenna 252 is shown with its expanded ground screen of  $20\text{ m} \times 20\text{ m}$ . The original  $3\text{ m} \times 3\text{ m}$  ground screen is shown instead for antenna 254, with white lines at the borders to guide the eye.

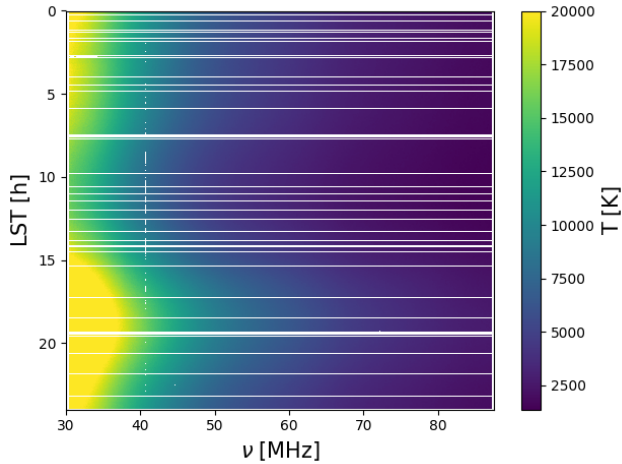


**Figure 3.** Waterfall plot example of a 24 h observation of antenna 254A in December 2018, in the full 30 – 87 MHz frequency range. The frequency resolution is 24 kHz and time resolution is  $\sim 15$  s. Note the amplitude variations, particularly visible at low frequencies, and around LST  $\sim 17$  h, when the Galactic center is transiting. White lines indicate RFI flagged data.

each frequency channel, we plot the relative variation of the observed temperature, calculated against the time average over  $N$  days:

$$\bar{T}(\nu) = \frac{1}{N} \sum_{d=1}^N T_d(\nu), \text{ with } N = 137. \quad (1)$$

Temporal variations are frequency-dependent in both antennas, with larger effects at low frequencies. We mark them in the Figure with red vertical lines and define in this way six different *datasets*, where temperature remains fairly constant with time. Despite a less sharp change of trend, we kept the data of May 2018 separated from the ones of December 2018. We recall that the December/January data are our *reference* dataset due to the seasonal optimal conditions for humidity and rainfall. The time discontinuities appear more evident in antenna 252A although contained at few % level, reaching 10–20% only at the lowest frequencies ( $\nu < 60$  MHz).

We then study the variation over time of the spectra measured by the two antennas. We show in Figure 5 the relative difference with respect to the mean value  $\bar{T}$ , computed by averaging all measured spectra. We plot the six *datasets* defined above with different colors. The 254A data show good stability; for frequencies higher than 60 MHz, within-datasets and between-datasets differences are

at most 5% and do not evolve much with frequency. Below 60 MHz, the different trends highlighted in Figure 4 are again clearly visible, leading to differences up to 10%. Antenna 252A has good consistency within each dataset, while differences across datasets can be as high as 30%. These latter are due both to temporal offsets as well as low frequency variations, visible in Figure 4 also. Differences are smaller at higher frequencies. We note that antenna 252A has a particularly marked discontinuity between January and February, corresponding to maintenance activities.

### 3 BEAM CHROMATICITY

The spectral smoothness of the foreground emission is the key property that should allow the retrieval of the 21 cm signal. Regardless of the parametrization used for the foregrounds, a frequency-dependent response of the antenna could corrupt their intrinsic spectra and thus prevent the extraction of the global signal (e.g. Bernardi et al. 2015; Mozdzen et al. 2016; Tauscher et al. 2020; Anstey et al. 2020). This beam chromaticity effect, however, can be (at least) partially compensated for by assuming an antenna beam and a foreground model (e.g. Mozdzen et al. 2017, 2019).

#### 3.1 Beam model

We use the NEC-4 package<sup>4</sup> that employs a method of moments to simulate an isolated dipole with a  $3\text{ m} \times 3\text{ m}$  mesh ground screen, a  $200\ \Omega$  load seen by the antenna at its interface with the receiver and a constant soil conductivity of  $0.005\text{ S m}^{-1}$ . The conductivity value is somewhat more representative of the December/January drier period.

Simulations were used to constrain an analytical beam model (Dowell 2011; Ellingson et al. 2013; Bernardi et al. 2015):

$$B(\nu, \hat{\mathbf{n}}) = \sqrt{[p_E(\theta, \nu) \cos \phi]^2 + [p_H(\theta, \nu) \sin \phi]^2},$$

where  $\hat{\mathbf{n}} = (\theta, \phi)$ ,  $E$  and  $H$  are the two orthogonal polarizations of the dipole and

$$p_i(\nu, \theta) = \left[ 1 - \left( \frac{\theta}{\pi/2} \right)^{\alpha_i(\nu)} \right] (\cos \theta)^{\beta_i(\nu) + \gamma_i(\nu)} \left( \frac{\theta}{\pi/2} \right) (\cos \theta)^{\delta_i(\nu)} \quad (2)$$

<sup>4</sup> <https://ipo.llnl.gov/technologies/software/nec-v50-numerical-electromagnetic-code>

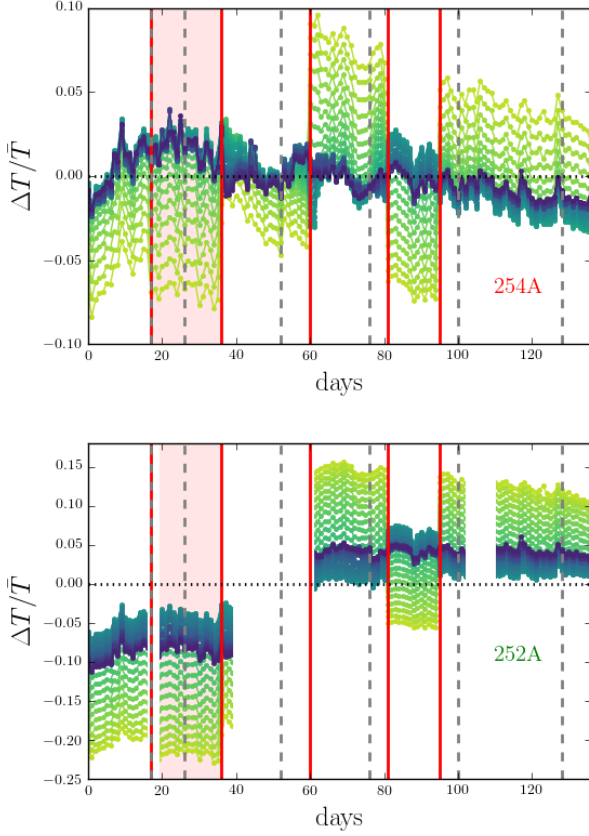


**Figure 4.** Variations of the measured sky temperature from antenna 254A (upper panel) and 252A (lower panel), as a function of observing day, plotted as a relative difference with respect to its mean value  $\bar{T}$  (equation 1). Different colors indicate different frequencies: lower (higher) frequencies are shown in lighter greens (darker blues). Dashed vertical lines denote the separation between months. May 2018 appears at the beginning of the x axis (note the dashed line superimposing with the first red vertical line), followed by December 2018 up to May 2019. Note that observations do not span all days of every month, therefore the number of days between two consecutive vertical dashed lines is smaller than 30. The relative temperature shows time discontinuities common to both antennas, more pronounced at low frequencies. These are highlighted in the plot with red vertical lines and define the six different *datasets*. Note that, despite a less prominent discontinuity, we keep May 2018 separated from December 2018. Our *reference* dataset are December 2018 and January 2019, marked as a red shaded region.

with  $i = E, H$ . The value of the coefficients  $[\alpha_i, \beta_i, \gamma_i, \delta_i]$  are fitted with an 11-th order polynomial.

A projection of the resulting beam in celestial coordinates can be found in Figure 6.

### 3.2 Foreground model

We first consider the Haslam 408 MHz sky map  $T_H(\hat{n})$  (Haslam et al. 1982) to model foregrounds and scale it to any frequency  $\nu$  with a constant spectral index across the entire sky, after subtracting the CMB temperature ( $T_{\text{cmb}} = 2.725$  K):

$$T_{\text{sky}}^H(\nu, \hat{n}) = [T_H(\hat{n}) - T_{\text{cmb}}] \left( \frac{\nu}{408} \right)^{-2.5} + T_{\text{cmb}}. \quad (3)$$

A second foreground model is derived from the 45 MHz Guzmán sky map  $T_G(\hat{n})$  (Guzmán et al. 2011). As this map misses data at

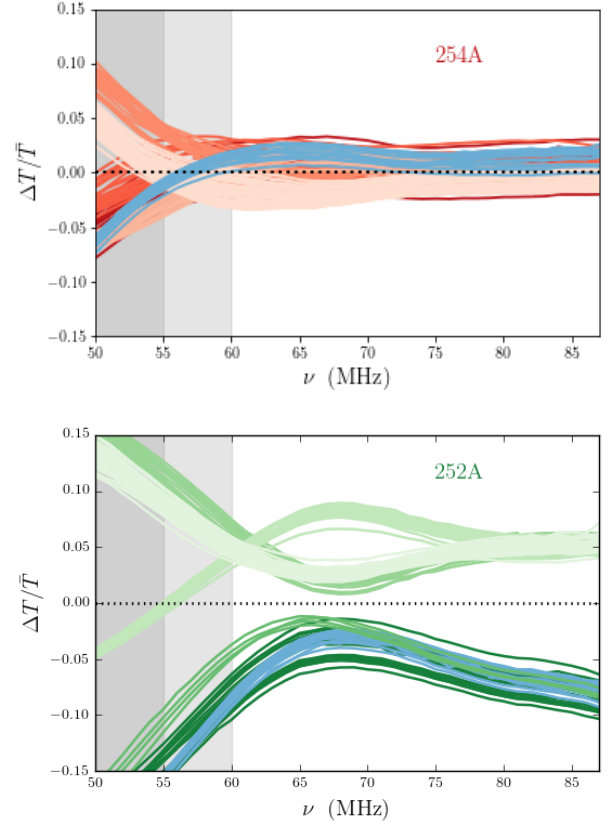


**Figure 5.** Time variation of the sky spectra measured by antenna 254A (upper panel) and 252A (lower panel), plotted as the relative difference with respect to the mean value  $\bar{T}$  - each color is a different *dataset* as defined in Figure 4. Chronologically earlier (later) datasets are shown in darker (lighter) colors (red for antenna 254A and green for antenna 252A). The *reference* dataset appears in blue in both plots in order to facilitate its identification. Gray shaded areas identify the lowest frequencies (dark gray  $\nu < 55$  MHz, light gray  $\nu < 60$  MHz).

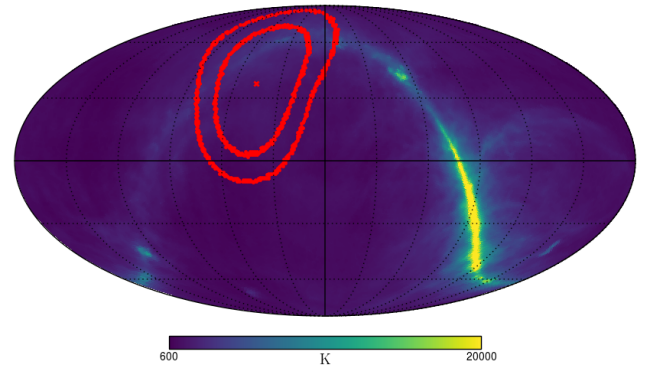


**Figure 6.** Red ellipses show -1dB and -2dB projection, in celestial coordinates, of the E-W oriented LEDA antenna model at 75 MHz, shown at LST = 3. The Haslam 408 MHz map scaled at 75 MHz with a constant spectral index of  $-2.5$  is shown in the background for illustration purposes. As the sky drifts the antenna is seeing different structures at the different LSTs.

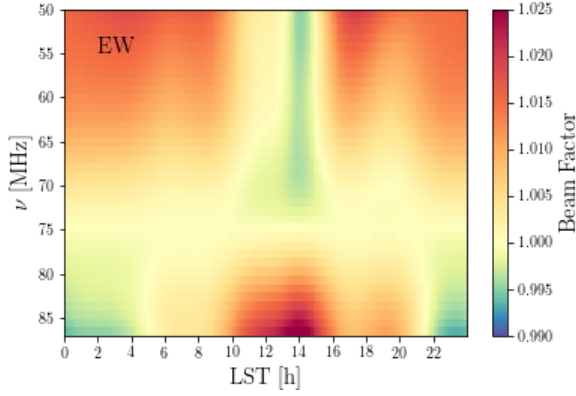


**Figure 7.** Beam chromaticity correction for a simulated E-W oriented LEDA antenna (pol A) as a function of frequency and LST. See text for details.

declination  $\delta > 65^\circ$ , we inpaint this empty region using  $T_{\text{sky}}^H(\nu_{45}, \hat{\mathbf{n}})$ . We call the resulting map  $\tilde{T}_G(\hat{\mathbf{n}})$ . We can compute from the Haslam and (inpainted) Guzman maps a more accurate "wide-band" spectral index  $\beta_{GH}(\hat{\mathbf{n}})$ :

$$\beta_{GH}(\hat{\mathbf{n}}) = \ln \frac{\tilde{T}_G^H(\hat{\mathbf{n}})}{T_{\text{sky}}^H(\hat{\mathbf{n}})} \left( \ln \frac{45}{408} \right)^{-1}. \quad (4)$$

The final sky model is constructed similarly to equation 3:

$$T_{\text{sky}}^G(\nu, \hat{\mathbf{n}}) = [\tilde{T}_G(\hat{\mathbf{n}}) - T_{\text{cmb}}] \left( \frac{\nu}{45} \right)^{\beta_{GH}(\hat{\mathbf{n}})} + T_{\text{cmb}}. \quad (5)$$

### 3.3 Beam chromaticity correction

The beam chromaticity correction can be computed as:

$$B_c(\nu, \text{LST}) = \frac{\int_{\Omega} T_{\text{sky}}(\nu_0, \text{LST}, \hat{\mathbf{n}}') B(\nu, \hat{\mathbf{n}}') d\hat{\mathbf{n}}'}{\int_{\Omega} T_{\text{sky}}(\nu_0, \text{LST}, \hat{\mathbf{n}}') B(\nu_0, \hat{\mathbf{n}}') d\hat{\mathbf{n}}'}. \quad (6)$$

Note that  $T_{\text{sky}}$  is a function of LST since the sky drifts with time over the antenna. We choose  $\nu_0 = 75$  MHz for the reference frequency in order to compare our results with [Mozdzen et al. \(2019\)](#). Note that this is a reasonable choice for us regardless, since it is a quite central frequency for the range of our data. We compute the beam chromaticity using our beam model (Section 3.1) and both the sky model of equation 3 and equation 5. We find very similar results, differing almost everywhere by less than a few tenths of a percent. The disagreement is slightly more pronounced closer to the Galactic center direction, but never higher than 1%.

In Figure 7 we present results using the Haslam sky model to show consistency with Figure 3 of [Mozdzen et al. \(2019\)](#).

For our final analysis we compute the chromaticity correction using  $T_{\text{sky}}^G$  and for each LST and frequency we use  $B_c(\nu, \text{LST})$  to correct our spectra:

$$T_c^{\text{obs}}(\nu, \text{LST}) \equiv T^{\text{obs}}(\nu, \text{LST}) / B_c(\nu, \text{LST}). \quad (7)$$

## 4 ABSOLUTE TEMPERATURE SCALE

We investigate the behavior of the chromaticity corrected spectra  $T_c^{\text{obs}}(\nu, \text{LST})$  as a function of LST, over the 24 hour range (Figure 8, 9). We focus on the *reference* dataset defined in Section 2 and

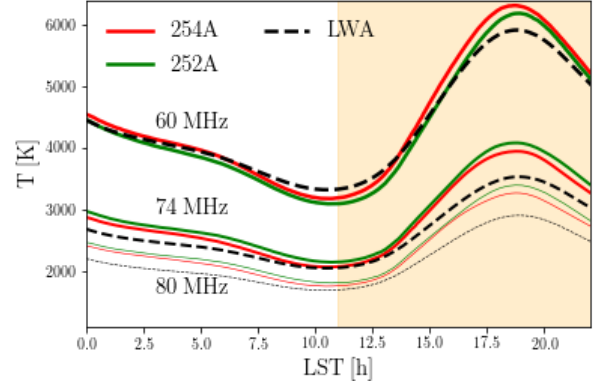


**Figure 8.** Comparison between the *reference* dataset mean sky temperature as a function of LST (antenna 254A in red and 252A green) with the average values of the LWA maps weighted by antenna response (black, see text for details) at 60, 74 and 80 MHz. For illustrative purposes, the light yellow shaded area indicates daylight, starting approximately from sunrise.

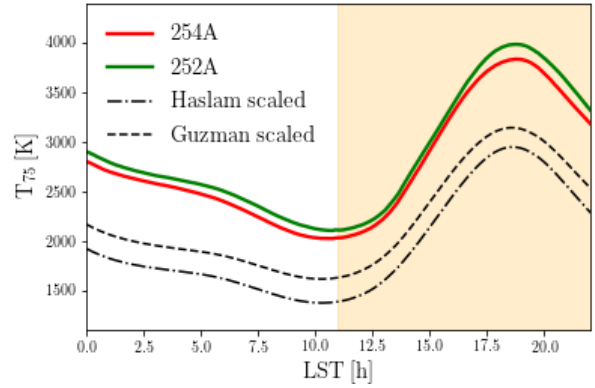


**Figure 9.** The averaged sky temperature measured by the antennas 254A (red) and 2542A (green) at 75 MHz as a function of LST for the *reference* dataset. For illustrative purposes, the light yellow shaded area indicates daylight, starting approximately from sunrise. In the Figure we also report the expected behavior of the sky temperature at 75 MHz extrapolated from other existing measurements. See text for details.

Figure 4. The measured sky temperature is consistent for the two antennas: it has a minimum in the LST range 10 – 12 h and reaches its peak around LST  $\sim 18$  h, when the Galactic center is closer to the visible sky.

We compare our results against existing foreground models and measurements by evaluating a simulated antenna temperature:

$$T^{\text{ant}}(\nu, \text{LST}) = \frac{\int_{\Omega} T_{\text{sky}}(\nu, \text{LST}, \hat{\mathbf{n}}) B(\nu_0, \hat{\mathbf{n}}) d\hat{\mathbf{n}}}{\int_{\Omega} B(\nu_0, \hat{\mathbf{n}}) d\hat{\mathbf{n}}}, \quad (8)$$

where  $T_{\text{sky}}$  are, alternatively LWA1 Low Frequency Sky Survey results ([Dowell et al. 2017](#)), the Haslam sky model,  $T_{\text{sky}}^H$  (equation 3), or the Guzman sky model,  $T_{\text{sky}}^G$  (equation 5). Note that we use the beam pattern at the reference frequency  $\nu_0 = 75$  MHz in order to avoid the introduction of chromaticity effects.

[Dowell et al. \(2017\)](#) have corrected their LWA interferometric ob-



servations with the sky-averaged temperature measured in December 2014 by the LEDA prototype system, LEDA-64 New Mexico deployment (Taylor et al. 2012; Schinzel et al. 2018). In Figure 8, we report the 60, 74 and 80 MHz frequencies and compare with our chromaticity corrected measurements of the sky temperature obtained with antenna 254A and antenna 252A. Their trend with LST is very similar and absolute values are consistent within  $\sim 10\%$ .

In Figure 9 we compare our measured temperature at 75 MHz for both antennas against the simulated temperature  $T^{\text{ant}}(75 \text{ MHz, LST})$  (equation 8), where we use either the Haslam sky model  $T_{\text{sky}}^{\text{H}}$  or the Guzman sky model  $T_{\text{sky}}^{\text{G}}$ . Predictions and our measurements have a comparable behavior with LST, however, they are discrepant in the absolute temperature scale. Although future analysis will be dedicated to investigating the precision of the absolute calibration, in this work we correct our absolute temperature scale to match the extrapolation from the 45 MHz map.

Figure 10 shows  $T_{\text{off}}(\nu)$ , i.e the difference between all our spectra (corrected for the chromaticity factor) and  $T_{\text{sky}}^{\text{G}}$  at LST = 12 h:

$$T_{\text{off}}(\nu) \equiv T_c^{\text{obs}}(\nu, \text{LST} = 12\text{h}) - T_{\text{sky}}^{\text{G}}(\nu, \text{LST} = 12\text{h}). \quad (9)$$

The offset is relatively constant with frequency and observing day. The strongest differences at low frequencies highlight the different *datasets* defined in Figure 4. An oscillatory pattern in  $T_{\text{off}}(\nu)$  with a period of approximately 20 MHz, common to both antennas, and visible across all the observations, can be tentatively inferred from Figure 10, indicating a possible systematic effect still present in the data.

Offset values for antenna 254A closely follow a Gaussian distribution for each *dataset*, and the standard deviation becomes smaller if we restrict the range to 60 – 87 MHz.

The offset values for antenna 252A span a larger range, as can be seen also in Figure 10, and their distribution deviates more significantly from a Gaussian profile. We retain for both antennas only  $T_{\text{off}}(\nu)$  in the 60 – 87 MHz range and we fit the various distributions with a Gaussian profile to obtain a mean  $\bar{T}_{\text{off}}$  and standard deviation value for each *dataset*. The best-fit mean and standard deviation are reported in Figure 11 for both antennas. The results for antenna 254A are quite stable along the duration of the observation while 252A shows a change of trend, consistently with what has been seen already in Figure 4 and 5. We correct our spectra by subtracting the mean value  $\bar{T}_{\text{off}}$  for each *dataset*.

## 5 SPECTRAL INDEX RESULTS

We now analyze our observations to characterize the spectral index of the foreground emission. We focus on our *reference* dataset in Section 5.1. We recall that for this dataset the observing conditions are optimal in terms of soil and rainfall. We study the spectral index averaging the spectra in LST bins of 5 minutes and across an LST range of  $\sim 24$  h. We concentrate instead on the 9 – 12.5 h LST range, that corresponds to the minimum of foreground contamination, when studying the six *datasets* in Section 5.2. Note that this LST range is the central interval of interest for further studies aimed at extracting a global signal constraint/upper limit. We model the data with a simple power law. Following Mozdzen et al. (2019) we write

$$T_{\text{m}}(\nu; \beta, T_{75}) = T_{75} \left( \frac{\nu}{\nu_{75}} \right)^{\beta} + T_{\text{cmb}}, \quad (10)$$

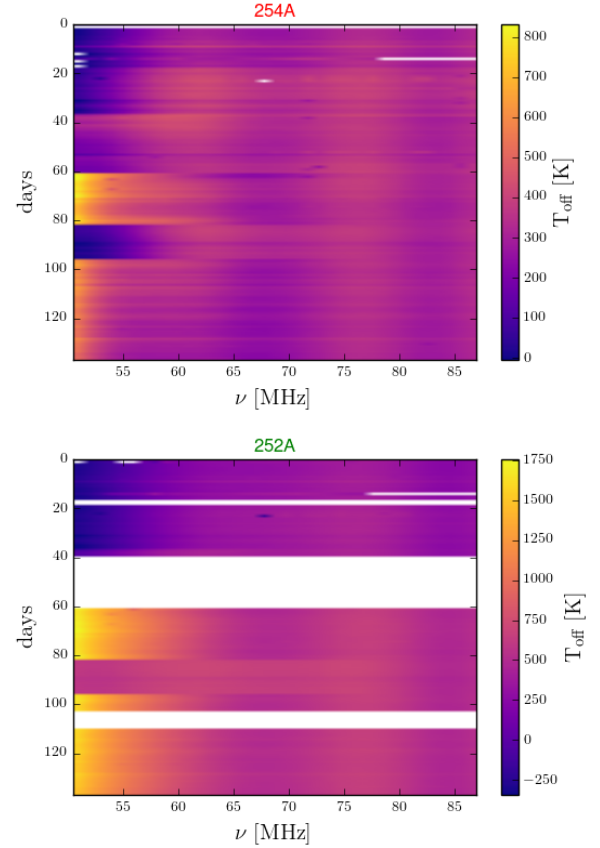


**Figure 10.** Offset temperature  $T_{\text{off}}(\nu)$  at LST = 12 h (see equation 9) for antenna 254A (upper panel) and 252A (lower panel) as a function of frequency and observing days. Note that the color bars have different extents for the two antennas. The difference among *datasets* is particularly evident at low frequency.

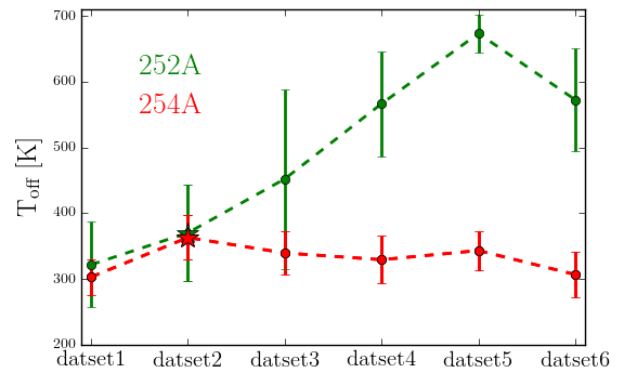


**Figure 11.** Mean values and  $1\sigma$  errors obtained from a Gaussian fit of the  $T_{\text{off}}$  distributions (Figure 10). The reference dataset is marked with a star.

choosing 75 MHz as a reference frequency. We perform a  $\chi^2$  minimization to constrain the model parameters for each LST bin:

$$\chi^2 = \sum_i \frac{[(T_c^{\text{obs}}(\nu_i) - \bar{T}_{\text{off}}) - T_m(\nu_i)]^2}{\sigma_i^2} \quad (11)$$

where  $N_f$  is the total number of 1 MHz frequency bins, and the errors  $\sigma_i$  correspond to the noise variance estimates discussed in Section 2.1. We recall that  $\bar{T}_{\text{off}}$  varies across datasets (Figure 11). In appendix A, we analyze the effect on the fit of the dispersion around this mean.

### 5.1 Reference dataset results

Figure 12 shows the best fit values of the spectral index as a function of LST and observing day.

Only data above  $\nu_{\text{min}} = 60$  MHz were used in the fit. We refer to appendix A for a discussion on the stability of the results with respect to this choice. We compute the RMS of the residuals for each LST bin and for each day, and report their values in the lower panels of Figure 12. We check for outliers in both  $\beta$  and RMS, and mask the corresponding spectra after a visual check. This procedure discards only few spectra.

Results are consistent across the observing window, highlighting the good stability of the instrument. The value of the spectral index  $\beta$  steepens around LST  $\sim 13$  h for both antennas. The smallest RMS values (around 20 K) occur in the 9 – 13 h LST range, motivating further the choice of this interval for the cosmological analysis. Similar trends are found for antenna 252A, although the RMS values are overall higher, reaching almost 100 K when the Galactic center is in the sky. Note that antenna 254A shows persistent variations at large LST values, in correspondence with high RMS values (around 30 K).

We show in Figure 13 the value of the mean spectral index as a function of LST and its variance across the different days of the dataset. The two antennas show similar trends although their results are slightly offset, with antenna 252A pointing toward a flatter  $\beta$ , as visible also from the upper panels of Figure 12. The mean spectral index shows almost no dependence on LST in the range 0 – 10 h for antenna 254A and in the range 5 – 10 h for antenna 252A. It then becomes steeper for both antennas around LST  $\sim 13$  h. Antenna 252A shows an almost constant spectral index for LST  $> 15$  h, while we can recognize the more complex pattern discussed above for antenna 254A. We report in Table 1 the mean value of the spectral index and its standard deviation averaged in LST bins of 3 h.

We compare our results with existing measurements and simulations. Following Mozdzen et al. (2019), we first compute a spectral index from the comparison of the Haslam and the Guzman maps:

$$\beta_{\text{GH}}(\text{LST}) = \ln \frac{T^{\text{ant}}(\nu_{45}, \text{LST})}{T^{\text{ant}}(\nu_{408}, \text{LST})} \left( \ln \frac{45}{408} \right)^{-1}, \quad (12)$$

where  $T^{\text{ant}}(\nu, \text{LST})$  is the portion of the sky model seen through the beam as the sky drifts, and thus is a function of LST. Moreover, we consider both the improved version of the GSM (Zheng et al. 2016) and the GMOSS (Sathyanarayana Rao et al. 2017) to create a set of full sky maps in the 60 – 87 MHz range, with 1 MHz spacing. We then simulate an observation with our antenna beam and consider LST values 10 minutes apart. We construct with this procedure a mock spectrum  $T^{\text{ant}}(\nu, \text{LST})$  for every LST value. Note that we consider the beam shape at the reference frequency of 75 MHz to avoid introducing chromaticity effects. We then perform a  $\chi^2$  minimization to constrain the model parameters of equation 10 for each LST bin, and report the best-fit spectral index in Figure 13.

**Table 1.** Spectral index  $\beta$  (equation 10) averaged in 3 h LST bins from the *reference* dataset. Errors  $\Delta\beta$  are computed from the standard deviation of all the spectra. The RMS is also the mean of the RMS values within each bin.

LST (h)	254 A			252 A		
	$\beta$	$\Delta\beta$	RMS (K)	$\beta$	$\Delta\beta$	RMS (K)
0-3	-2.55	0.01	25.08	-2.51	0.02	112.37
3-6	-2.55	0.01	21.99	-2.46	0.02	94.14
6-9	-2.54	0.01	21.90	-2.43	0.02	82.58
9-12	-2.54	0.01	20.70	-2.44	0.02	79.05
12-15	-2.58	0.01	23.31	-2.46	0.02	93.77
15-18	-2.57	0.01	29.33	-2.45	0.02	135.40
18-21	-2.58	0.01	26.96	-2.46	0.02	153.21

The overall variation with LST of these models and of  $\beta_{\text{GH}}(\text{LST})$  is in good agreement with the one found in our data. Note for example the steeper spectral index around LST  $\sim 13$  h. It is worth noticing that the best-fit values for the scaling temperature  $T_{75}$  are well in agreement with their observed ones, once corrected for the offset. This assures that the best-fit solution is not falling in un-physical minima.

We also report in Figure 13 the results obtained without the beam factor correction, to assess its impact. The spectral index in this case is found to flatten when the sky temperature is minimal, in agreement with the results in Price et al. (2018), for which the beam chromaticity was not taken into account. The effect of the correction is stronger below LST  $\sim 5$  h and around LST  $\sim 13$  h.

### 5.2 All dataset results

We now analyze the value of the spectra index for the spectra in the 6 *datasets* defined in Section 2, following the same procedure of Section 5.1. Although the data show a coherent behavior on a time scale of few tens of days, there are changes throughout the months that reflect in different  $\bar{T}_{\text{off}}$  values for each dataset. Slight variations across *datasets* are thus expected for the best-fit values of the spectral index.

We report these values of  $\beta$  as a function of LST and observing day in Figure 14, and in Table 2 the mean and standard deviation for each dataset. We also report the averaged RMS values of the residuals. Note that, in the restricted LST range 9 – 12.5 h, we can enlarge the *reference* dataset with more spectra that we are otherwise obliged to discard when requiring high quality over the full 24 h range. For this reason *dataset2* has larger error bars than the one presented in Section 5.1.

We report in Figure 15 the mean and standard deviation obtained from Figure 14 for each dataset, as a function of LST. There is good consistency across datasets and we find similar variation as a function of LST, in particular for antenna 254A. We also report in the lower panels the variation of the RMS of the residuals. The RMS values are always lower for antenna 254A than for antenna 252A, as found for the case of the *reference* dataset.

As for Section 5.1, we do not report the best-fit value of  $T_{75}$  but we remark its agreement with the (offset corrected) measured value of the sky temperature at 75 MHz.



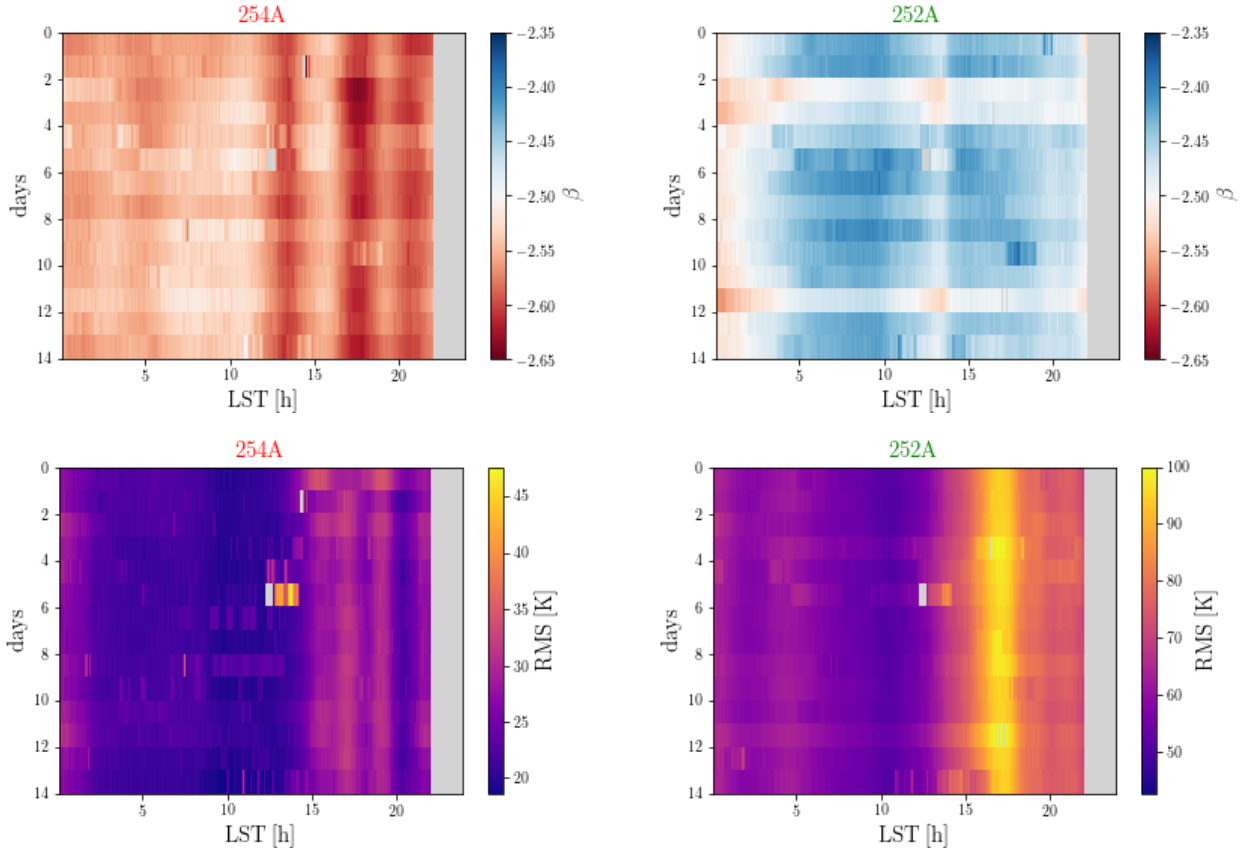


**Figure 12.** *Upper panels:* Best fit value for the  $\beta$  parameter of equation 10 for our *reference* dataset as a function of LST for the antenna 254A (left) and 252A (right). Note that the colorbar is the same for the two antennas to help the comparison. *Lower panels:* The RMS of the residual spectra for antenna 254A (left) and 252A (right).

**Table 2.** Mean of the best-fit spectral index  $\beta$  (equation 10) for each of the six *datasets*, obtained by averaging over the LST range 9 – 12.5 h. The quoted RMS values are averaged accordingly. The errors  $\Delta\beta$  are computed from the standard deviation of the spectra.

	254 A			252 A		
<i>dataset</i>	$\beta$	$\Delta\beta$	RMS (K)	$\beta$	$\Delta\beta$	RMS (K)
1	-2.47	0.01	19.32	-2.39	0.01	48.72
2 (ref)	-2.54	0.03	21.60	-2.47	0.10	44.88
3	-2.50	0.06	24.15	-2.66	0.09	52.86
4	-2.44	0.06	25.35	-2.63	0.08	60.20
5	-2.45	0.06	23.90	-2.65	0.09	58.11
6	-2.41	0.02	25.88	-2.58	0.02	59.30

## 6 SPECTRAL CURVATURE

We now investigate a possible curvature  $\gamma$  of the spectra index, comparing our data to the three parameter model:

$$T_m(\nu; \beta, \gamma, T_{75}) = T_{75} \left( \frac{\nu}{\nu_{75}} \right)^{\beta + \gamma \ln(\nu/\nu_{75})} + T_{\text{cmb}}. \quad (13)$$

We restrict our analysis to antenna 254A. One needs to be careful in opening up the parameter space since the non-smoothness of our spectra easily drive the fit toward un-physical values for the curvature  $\gamma$ . We present the results first for our *reference* dataset in Section 6.1

and then for the six *datasets* in the restricted LST range in Section 6.2. Note that, as it is defined in our model, a positive curvature ( $\gamma > 0$ ) would imply a steepening of the spectra at lower frequencies, while a negative one ( $\gamma < 0$ ) a flattening or absorption.

### 6.1 Reference dataset results

We apply the same procedure described in Section 5.1 to our *reference* dataset, except that we use equation 13 for the model  $T_m$  in the  $\chi^2$  minimization. The results for the mean and standard deviation of the best-fit values of  $\gamma$  as a function of LST are shown in Figure 16. We report in Table 3 the mean and standard deviation of the best-fit values of the spectral index  $\beta$  and the curvature parameter  $\gamma$ , averaged over 3 or 1 hours of LST bins.

We find a positive value of  $\gamma$ , paired with a flatter  $\beta$  at low LST ( $< 5$  h). This positive value for the curvature could be spurious: in the 0 – 5 h LST range the sky temperature is high since the beam is directly collecting signal from the Galactic Plane, implying that the results are more prone to systematics. Indeed, the tension with null curvature lowers in the LST range 5 – 10 h, and the curvature is consistent with zero in the range 10 – 12 h, as reported also in Table 3. When the Galactic center starts to enter the collecting area of the beam,  $\gamma$  shows strong variations. It first becomes again slightly positive reaching 0.4 although with large scatter across the various spectra. Then it drops to  $-0.4$  when the Galactic emission is strong (LST  $\sim 17$  h). Such a strong negative value for the curvature at low frequencies (150 MHz), is, for example, predicted by the GSM in De

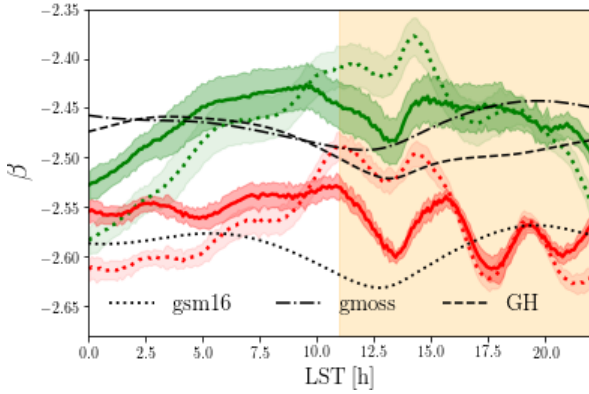


**Figure 13.** Mean value of the best fit daily spectral index  $\beta$ , as a function of LST, for the beam corrected reference dataset of Figure 12 (solid lines) compared with the non-corrected one (dotted lines), for the antenna 254A (in red) and 252A (in green). Shaded areas show the standard deviation. For comparison the Guzman-Haslam (black dashed), improved GSM (black dotted) and GMOSS (black dashed dotted) spectral index (see text for details) are also shown. For illustrative purposes, the shaded yellow area indicates daylight, starting approximately from sunrise.

**Table 3.** Mean values of the best-fit spectral index  $\beta$  and its curvature  $\gamma$  obtained for the 3 parameter model of equation 13 using the spectra of the reference dataset for antenna 254A. The results cover an almost 24 h LST range, averaged in LST bins of 3 h and refined to 1 h for LST > 15 h. The error  $\Delta\beta$  and  $\Delta\gamma$  are computed from the standard deviation of all the spectra considered. The RMS of the residuals is also averaged in the same LST bins.

LST (h)	$\beta$	$\Delta\beta$	$\gamma$	$\Delta\gamma$	RMS (K)
0-3	-2.53	0.01	0.28	0.06	23.23
3-6	-2.55	0.01	0.11	0.06	21.57
6-9	-2.53	0.02	0.18	0.07	21.14
9-12	-2.52	0.01	0.13	0.11	20.32
12-15	-2.56	0.01	0.13	0.13	22.63
15-16	-2.52	0.01	0.24	0.12	26.81
16-17	-2.59	0.01	-0.21	0.12	29.11
17-18	-2.63	0.02	-0.28	0.08	28.55
18-19	-2.59	0.01	-0.00	0.05	28.33
19-20	-2.57	0.01	0.011	0.04	29.00
20-21	-2.58	0.01	0.10	0.04	22.97

Oliveira-Costa et al. (2008) close the Galactic plane. Note that also in in Mozdzen et al. (2019) the result for the three parameter model shows a more negative curvature in the LST range 12 – 20 h.

## 6.2 All dataset results

In Table 4 we report the mean and standard deviation of the best-fit values for the spectral index and its curvature for each dataset averaged over the LST range 9 – 12.5h. Opening up the model to a third parameter modifies only minimally the best-fit value of  $\beta$  in this LST range and the mean values of  $\gamma$  are compatible with zero at  $\sim 2\sigma$  (see upper panel of Figure 17). The only noticeable difference is found for dataset1, where  $\gamma$  is slightly positive and, consequently,  $\beta$  tends to be flatter for the 3 parameter model. The RMS values for the residuals are also similar, although slightly lower, to the ones

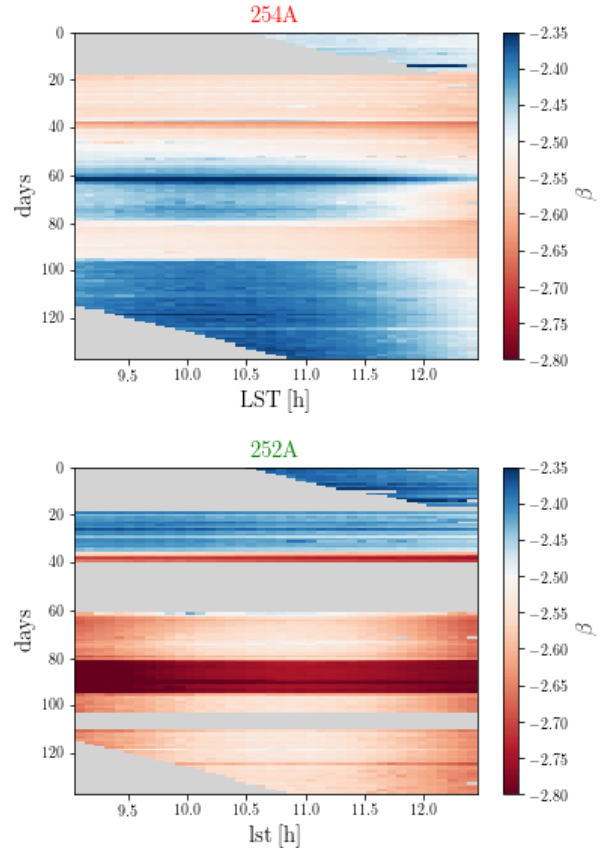


**Figure 14.** Best fit value for the  $\beta$  parameter of equation 10 for every day of our full dataset in the LST range 9-12.5 h (LST binning  $\sim 5$  mins) for the antenna 254A (upper panel) and 252A (lower panel). Note that data from May 2018 and 2019 do not cover the entire LST range, to avoid data too close to the sunset. The colorbar is the same for the two antennas to aid the comparison.

obtained for the 2 parameter model (see lower left panel of Figure 15). The stability of the spectral index going from 2 to 3 parameters is a good indication for the quality of the data.

## 7 DISCUSSION AND CONCLUSIONS

We presented the analysis of LEDA radiometric data with the aim of measuring the spectral index of Galactic radio emission in the 60–87 MHz range. Observations were carried out with two antennas (252A and 254A) and spanned a total of  $\sim 600$  hours divided in six different datasets covering May 2018 and from December 2018 to May 2019.

Observed spectra were corrected for the effect of beam chromaticity following Mozdzen et al. (2017, 2019) and re-scaled to be in agreement with the absolute temperature scale derived from existing observations of Guzmán et al. (2011); Haslam et al. (1982). The beam chromaticity effect leads to spectral index corrections of no more than  $\sim 4\%$ . We note here that an approach that incorporates beam effects in the foreground model and, therefore, bypasses the chromaticity correction, has recently been discussed in the literature (Tauscher et al. 2020; Anstey et al. 2020), although not applied to observations yet.

We found that the spectral index is fairly flat across 24 h LST range.

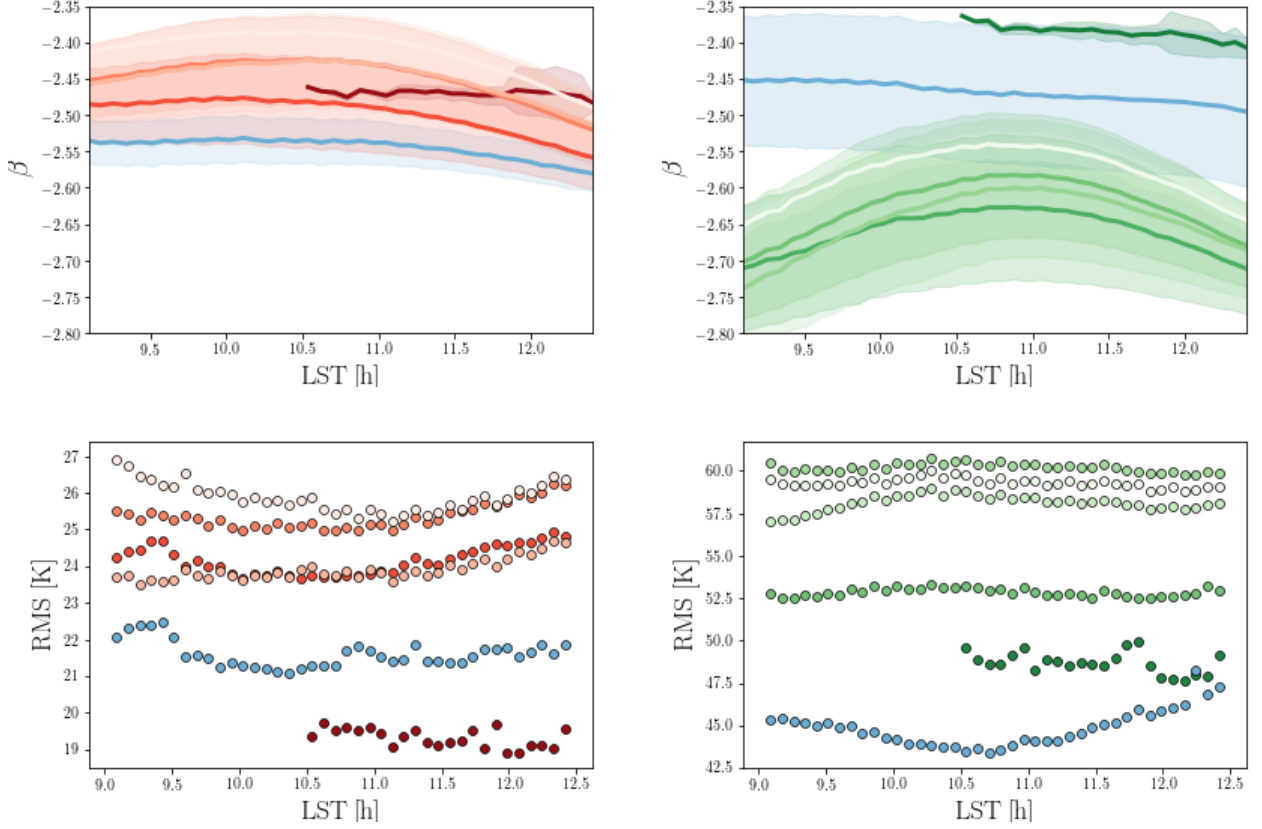


**Figure 15.** *Upper panel:* Mean and standard deviation of the best fit values of  $\beta$  of Figure 14 split between the different datasets defined in Section 2, color coded as in Figure 5, for antenna 254A (left, red scale) and antenna 252 (right, green scale). *Lower panel:* Mean RMS for the residuals for antenna 254A (left) and 252A (right). Every marker represents a different LST bin ( $\sim 5$  min large) color coded to identify the different datasets. The *reference* dataset is reported in blue to facilitate identification.

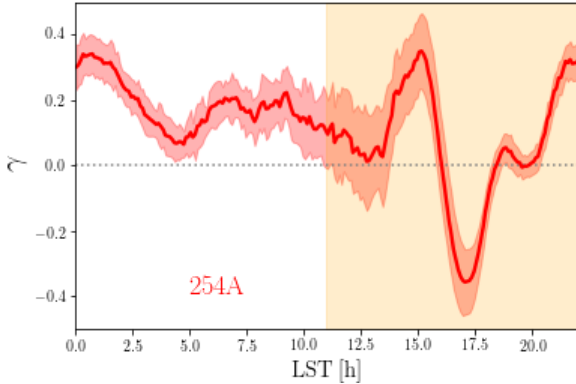


**Figure 16.** Mean value of the best fit spectral index curvature  $\gamma$  (see equation 13), as a function of LST, for the beam corrected *reference* dataset for antenna 254A. The shaded area shows the standard deviation. As for some of the previous Figures, the shaded yellow area indicates daylight, starting approximately from sunrise.

It varies from  $\beta = -2.55 \pm 0.01$  for antenna 254A at LST  $< 6$  h to  $\beta = -2.58 \pm 0.01$  at LST  $\sim 13$  h. A similar behavior is found for antenna 252A, although with a flatter mean spectral index, changing

**Table 4.** Best-fit values of the spectral index  $\beta$  and its curvature  $\gamma$  obtained for the 3 parameter model of equation 13 using the spectra of the antenna 254A divided between the 6 different datasets defined in Section 2. The error  $\Delta\beta$  and  $\Delta\gamma$  are computed from the standard deviation of all the spectra considered in each dataset. The RMS is computed from the residuals with respect of the model. We reiterate that the data are selected to span the LST range 9–12.5 h only.

dataset	$\beta$	$\Delta\beta$	$\gamma$	$\Delta\gamma$	RMS (K)
1	-2.44	0.01	0.23	0.10	18.77
2 (ref)	-2.53	0.03	0.18	0.12	21.23
3	-2.50	0.06	0.03	0.28	23.45
4	-2.44	0.07	0.10	0.27	24.50
5	-2.44	0.08	0.10	0.27	23.02
6	-2.39	0.02	0.21	0.17	25.06

from  $\beta = -2.43 \pm 0.02$  to  $\beta = -2.46 \pm 0.02$ . Residual rms values after subtracting the best fit power law vary from 20 – 30 K for antenna 254A to 70 – 150 K for antenna 252A.

Our results are broadly consistent with previous measurements. Guzmán et al. (2011) derived a spectral index map from 45 MHz and 408 MHz with  $-2.6 < \beta < -2.5$  over most of the sky. Similarly, Mozdzen et al. (2019) found  $-2.59 < \beta < -2.54$  at LSTs from 0 to 12 h in the 50 – 100 MHz range, flattening to  $\beta = -2.46$  when

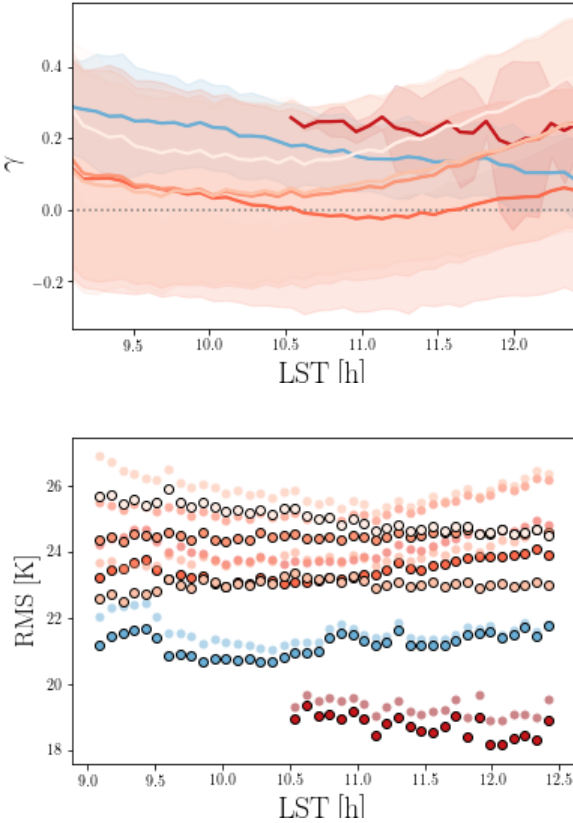


**Figure 17.** *Upper panel:* Mean and standard deviation of the best fit values of the curvature  $\gamma$  for the model of equation 13 split in the different datasets defined in Section 2, color coded as in Figure 5, for antenna 254A. *Lower panel:* Mean of the RMS of the residuals for the model including curvature (black edged colored markers) compared with the values of Figure 15 (plain markers). Every point is for a different LST bin ( $\sim 5$  min large) and color coded to distinguish the different datasets.

the Galactic center is transiting - although their observations cover the southern celestial hemisphere and can, therefore, only be qualitatively compared to ours. Moreover, we find broad agreement with the Improved GSM (Zheng et al. 2016) and GMOSS (Sathyanarayana Rao et al. 2017) sky models.

We analyzed the full six *datasets* in the 9–12.5 h LST range, where the foreground temperature shows a minimum. The distribution of the best fit spectral indexes for antenna 254A spans values from  $-2.54$  to  $-2.41$ , all consistent with the mean  $\beta = -2.48 \pm 0.07$ . Spectral index are in general less stable for antenna 252A, leading to a mean value  $\beta = -2.57 \pm 0.12$ , all consistent, however, with the values from 254A within the  $2\sigma$  confidence interval.

We used data from the most stable antenna, 254A, to investigate the presence of curvature in the foreground spectrum. We found that all *datasets* are compatible with no curvature at  $1 - 2\sigma$  level in the 9 – 12.5 h range. We found instead some preference for a non zero curvature when studying LST values outside this range, possibly due to residual systematic effects. The relatively pronounced curvature at LST  $\sim 17^{\text{h}}$ , may have a physical interpretation as due to self absorption from HII regions in the Galactic center area, which was also tentatively pointed out by Mozdzen et al. (2019).

## ACKNOWLEDGEMENTS

The authors kindly thank the Caltech OVRO staff for the great dedication and skills demonstrated in constructing the LWA array. MS acknowledges funding from the INAF PRIN-SKA 2017 project 1.05.01.88.04 (FORECaST) and support from the INFN INDARK PD51 grant. AF is supported by the Royal Society University Research Fellowship. LEDA research has been supported in part by NSF grants AST/1106059, PHY/0835713, and OIA/1125087. The OVRO-LWA project was enabled by the kind donation of Deborah Castleman and Harold Rosen.

## References

- Anstey D., de Lera Acedo E., Handley W., 2020, arXiv e-prints, p. [arXiv:2010.09644](https://arxiv.org/abs/2010.09644)
- Barkana R., 2018, *Nature*, **555**, 71
- Barkana R., Loeb A., 2005, *ApJ*, **626**, 1
- Bernardi G., McQuinn M., Greenhill L. J., 2015, *ApJ*, **799**, 90
- Bernardi G., et al., 2016, *Monthly Notices of the Royal Astronomical Society*, **461**, 2847
- Bevins H. T. J., Handley W. J., Fialkov A., de Lera Acedo E., Greenhill L. J., Price D. C., 2020, arXiv e-prints, p. [arXiv:2007.14970](https://arxiv.org/abs/2007.14970)
- Bowman J. D., Rogers A. E. E., Monsalve R. A., Mozdzen T. J., Mahesh N., 2018, *Nature*, **555**
- Cohen A., Fialkov A., Barkana R., Lotem M., 2017, *MNRAS*, **472**, 1915
- De Oliveira-Costa A., Tegmark M., Gaensler B. M., Jonas J., Landecker T. L., Reich P., 2008, *MNRAS*, **388**, 247
- Dowell J., 2011, Parametric Model for the LWA-1 Dipole Response as a Function of Frequency
- Dowell J., Taylor G. B., Schinzel F. K., Kassim N. E., Stovall K., 2017, *MNRAS*, **469**, 4537
- Eastwood M. W., et al., 2018, *The Astronomical Journal*, **156**, 32
- Ellingson S. W., Craig J., Dowell J., Taylor G. B., Helmboldt J. F., 2013, arXiv e-prints, p. [arXiv:1307.0697](https://arxiv.org/abs/1307.0697)
- Fialkov A., Barkana R., Visbal E., Tseliakhovich D., Hirata C. M., 2013, *MNRAS*, **432**, 2909
- Fialkov A., Barkana R., Visbal E., 2014, *Nature*, **506**, 197
- Field G. B., 1958, *Proceedings of the IRE*, **46**, 240
- Furlanetto S. R., Oh S. P., Briggs F. H., 2006, *Phys. Rep.*, **433**, 181
- Guzmán A. E., May J., Alvarez H., Maeda K., 2011, *A&A*, **525**, A138
- Harker G. J. A., Mirocha J., Burns J. O., Pritchard J. R., 2016, *MNRAS*, **455**, 3829
- Haslam C. G. T., Salter C. J., Stoffel H., Wilson W. E., 1982, *A&AS*, **47**, 1
- Hills R., Kulkarni G., Meerburg P. D., Puchwein E., 2018, *Nature*, **564**, E32
- Kocz J., et al., 2015, *Journal of Astronomical Instrumentation*, **4**, 1550003
- Landecker T. L., Wielebinski R., 1970, *Australian Journal of Physics Astrophysical Supplement*, **16**, 1
- McKinley B., et al., 2018, *MNRAS*, **481**, 5034
- Mesinger A., Ferrara A., Spiegel D. S., 2013, *MNRAS*, **431**, 621
- Mesinger A., Greig B., Sobacchi E., 2016, *MNRAS*, **459**, 2342
- Mirocha J., 2014, *MNRAS*, **443**, 1211
- Mirocha J., Furlanetto S. R., 2019, *MNRAS*, **483**, 1980
- Mozdzen T. J., Bowman J. D., Monsalve R. A., Rogers A. E. E., 2016, *MNRAS*, **455**, 3890
- Mozdzen T. J., Bowman J. D., Monsalve R. A., Rogers A. E. E., 2017, *MNRAS*, **464**, 4995
- Mozdzen T. J., Mahesh N., Monsalve R. A., Rogers A. E. E., Bowman J. D., 2019, *MNRAS*, **483**, 4411
- Offringa A. R., de Bruyn A. G., Biehl M., Zaroubi S., Bernardi G., Pandey V. N., 2010, *MNRAS*, **405**, 155
- Patra N., Subrahmanyan R., Sethi S., Shankar N. U., Raghunathan A., 2015, *The Astrophysical Journal*, **801**, 138
- Philip L., et al., 2019, *Journal of Astronomical Instrumentation*, **8**, 1950004
- Price D. C., et al., 2018, *MNRAS*, **478**, 4193
- Pritchard J. R., Furlanetto S. R., 2007, *MNRAS*, **376**, 1680



- Pritchard J., Loeb A., 2010, *Nature*, **468**, 772
- Rogers A., Bowman J., 2008, *Astron. J.*, 136
- Sathyanarayana Rao M., Subrahmanyam R., Udaya Shankar N., Chluba J., 2017, *AJ*, **153**, 26
- Schinkel F., et al., 2018, A Prototype Lower-VHF Radiometry System at the Long Wavelength Array
- Shaver P. A., Windhorst R. A., Madau P., de Bruyn A. G., 1999, *A&A*, **345**, 380
- Sims P. H., Pober J. C., 2020, *MNRAS*, **492**, 22
- Singh S., Subrahmanyam R., 2019, *The Astrophysical Journal*, **880**, 26
- Singh S., et al., 2017, *ApJ*, **845**, L12
- Singh S., Subrahmanyam R., Shankar N. U., Rao M. S., Girish B. S., Raghunathan A., Somashekar R., Srivani K. S., 2018, *Experimental Astronomy*, **45**, 269
- Sokolowski M., et al., 2015, *Publications of the Astronomical Society of Australia*, **32**, e004
- Spinelli M., Bernardi G., Santos M. G., 2019, *MNRAS*, **489**, 4007
- Tauscher K., Rapetti D., Burns J. O., 2020, *ApJ*, **897**, 132
- Taylor G. B., et al., 2012, *Journal of Astronomical Instrumentation*, **01**, 1250004
- Venkatesan A., Giroux M. L., Shull J. M., 2001, *ApJ*, **563**, 1
- Voytek T. C., Natarajan A., Jáuregui García J. M., Peterson J. B., López-Cruz O., 2014, *ApJ*, **782**, L9
- Wouthuysen S. A., 1952, *AJ*, **57**, 31
- Zheng H., et al., 2016, *Monthly Notices of the Royal Astronomical Society*, **464**, 3486

## APPENDIX A: STABILITY OF THE RESULTS ON THE SPECTRAL INDEX

We perform some further tests to assess the stability of our measured spectral indices. We concentrate on the results of Section 5.1 which are the central ones of this work.

First we investigate the dependence of our findings with respect to the offset  $T_{\text{off}}$  discussed in Section 4 and reported in Figure 11. There is an expected correlation between the offset and the steepness of  $\beta$ : the larger the offset that is removed, the more we should obtain a steep  $\beta$ , since the subtraction is more effective at high frequencies, where the sky temperature is lower. We report results obtained considering the  $1\sigma$  deviation from the mean  $T_{\text{off}}$  in Figure A1. The result for every intermediate value falls in between these solutions for both antenna 254A and 252A. The reported variations shows a consistent trend with LST and deviations of no more than a few % for the overall value of the spectral index.

Our results for the spectral index have been obtained considering a minimum frequency cut at  $\nu_{\text{min}} = 60$  MHz for our spectra. This choice, already discussed in Section 2, minimizes the environmental effects in the data. We report in Figure A2 the best fit of the spectral index for the *reference* dataset obtained by lowering  $\nu_{\text{min}}$  to 55 or 50 MHz, for completeness. We find a flattening of the spectral index, expected when including these lower frequencies (e.g. De Oliveira-Costa et al. 2008) The effect is particularly strong for antenna 252A, reaching  $\beta \sim -2.15$ . Note however that the trend in LST is consistent for all frequency cuts. The results for antenna 254A are more stable, as also expected from Figure 5.

This paper has been typeset from a  $\text{\LaTeX}$  file prepared by the author.

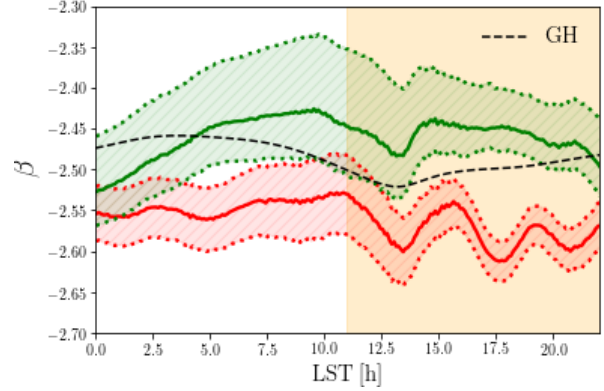


**Figure A1.** The mean value of the beam corrected best fit daily spectral index of Figure 13 (254A in red and 252A in green) compared with the best fit obtained from equation 11 substituting  $T_{\text{off}}$  with  $T_{\text{off}} + 1\sigma$  and  $T_{\text{off}} - 1\sigma$  from Figure 11 (dotted lines). The dashed area shows the range of values of  $\beta$  from intermediate values of  $T_{\text{off}}$ . For comparison the Guzman-Haslam spectral index is shown (black dashed line, see equation 12). For illustrative purposes, the shaded yellow area indicates daylight, starting approximately from sunrise.

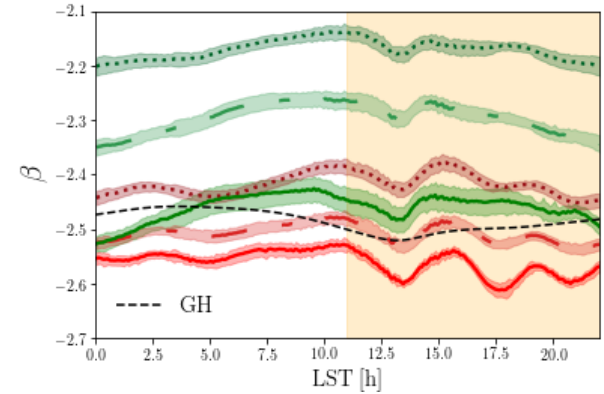


**Figure A2.** The mean value of the beam corrected best fit daily spectral index of Figure 13 (solid red line for antenna 254A and solid green for the 252A) compared with the best fit obtained by varying the minimum frequency considered in the fit, from the standard 60 MHz to 55 MHz (dot-dashed lines) and 50 MHz (dotted lines). The red and green shaded areas show the standard deviation. For comparison the Guzman-Haslam spectral index is shown (black dashed line, see equation 12). For illustrative purposes, the shaded yellow area indicates daylight, starting approximately from sunrise.